Magnetic structure and field-induced transitions in the triangular spin-1 antiferromagnet NiNb$_2$O$_6$: Observation of a triple point

Maruthi R [1,2] Sobhit Singh [3,4,*] Sayandeep Ghosh [5,6] Mohindar S. Seehra [7] Bruno Weise [8] Wilfrid Prellier [9] and Subhash Thota [1,9,†]

[1]*Department of Physics, Indian Institute of Technology, Guwahati, Assam 781039, India*
[2]*Department of Physics, B.M.S. College of Engineering, Bangalore 560019, Karnataka, India*
[3]*Department of Mechanical Engineering, University of Rochester, Rochester, New York 14627, USA*
[4]*Materials Science Program, University of Rochester, Rochester, New York 14627, USA*
[5]*Department of Physics, Chungnam National University, Daejeon 34134, Republic of Korea*
[6]*Department of Physics, Kunsan National University, Gunsan 54150, Republic of Korea*
[7]*Department of Physics & Astronomy, West Virginia University, Morgantown, West Virginia 26506, USA*
[8]*Leibniz-IFW Dresden, Institute for Complex Materials, D-01069 Dresden, Germany*
[9]*CRISMAT laboratory, Normandy University, ENSICAEN, UNICAEN, National Center for Scientific Research, 14000 Caen, France*

A comprehensive experiment-theory study on the magnetic field-induced spin-flip transitions (H_{C1} and H_{C2}) and the field-temperature (H-T) phase diagram of nickel niobate (NiNb$_2$O$_6$) polycrystals is reported. Magnetic susceptibility (χ) measurements reveal the presence of quasi-one-dimensional magnetism with spin-1 Ni^{2+} Heisenberg spin chains, instead of Ising chains, along the easy axis (c axis). The ferromagnetic intrachain exchange-interaction strength, J_0/k_B (=4.20 K), between Ni^{2+} ions in the c axis is estimated from the molecular-field theory approximation. The interchain exchange interactions $J_1/k_B = -1.335$ K and $J_2/k_B = -1.298$ K have been determined from the experimentally obtained magnitudes of $H_{C1} = 10.8$ kOe and spin-saturated field $H_S = 38$ kOe. These magnitudes are consistent with the total magnetic exchange-interaction strength, $J/k_B = 7.00$ K obtained from χ-T data fitted with the Heisenberg linear chain model and our density-functional theory (DFT+U) calculations. The overall antiferromagnetic behavior of the NiNb$_2$O$_6$ system, correctly captured within our DFT+U calculations, occurs below $T_N = 5.59 \pm 0.02$ K as determined from the analysis of the specific heat (C_P-T) data. The C_P vs T data near T_N is fitted to power-law expression $C_P = A|T - T_N|^{-\alpha}$ yielding the critical exponent $\alpha = 0.349(2)$ [0.349(1)] for $T > T_N$ ($T < T_N$), respectively. Further, the H-T phase diagram mapped for $H||c$ axis using various critical fields acquired from the $\chi(T, H)$ data including the field-induced transitions [$H_{C1}(T)$ and $H_S(T)$] yields a triple point, $T_{TP}(H, T) = (5.0$ kOe, 5.50 K) that separates multiple distinct spin configurations in this interesting system and calls for additional studies near the triple point. The companion H-T phase diagram for $H||a$ axis is also presented using the data collected from published sources.

I. INTRODUCTION

Quantum criticality, quantum phase transitions, and quantum fluctuations are emerging trends in the field of condensed matter physics. Consequently, there is a growing need to identify real materials that exhibit these quantum phenomena [1–5]. One such class of material is niobate columbites (CoNb$_2$O$_6$ and NiNb$_2$O$_6$) due to their novel quantum magnetic critical characteristics and applications. The quantum phase transition near quantum critical point (QCP) has been experimentally reported in the niobate columbite CoNb$_2$O$_6$ (Ising magnet with effective spin $S = 1/2$) in the presence of a transverse magnetic field and is the closest realization of the transverse-field Ising chain model [6,7]. Recently, quantum critical excitations near QCP have also been reported in

NiNb$_2$O$_6$ (effective spin $S = 1$) in specific-heat and thermal conductivity measurements when the critical field $H_{QCP} \sim 35$ kOe is applied perpendicular to the easy axis [8,9]. Analogous to CoNb$_2$O$_6$ [6,7], NiNb$_2$O$_6$ in a transverse magnetic field is the closest real system for the transverse-field Heisenberg chain Hamiltonian with effective spin $S = 1$ ground state [8,9]. Besides, NiNb$_2$O$_6$ has also been reported as a potential candidate for photocatalysis under visible-light irradiation for efficient production of H$_2$ from water splitting [10]. The type of spin chain along the easy axis in NiNb$_2$O$_6$ system is not fully understood. Additionally, the estimation of the appropriate magnitudes of the magnetic exchange constants, as well as the role of their higher-order terms, in relation to the magnetic structure of this system, remains unclear. Moreover, the H-T phase diagram and spin-flip transitions in NiNb$_2$O$_6$ are not yet thoroughly explored.

The focus of this paper being complete mapping of the magnetic field-temperature (H-T) phase diagram of NiNb$_2$O$_6$ below its Néel temperature and determination of the

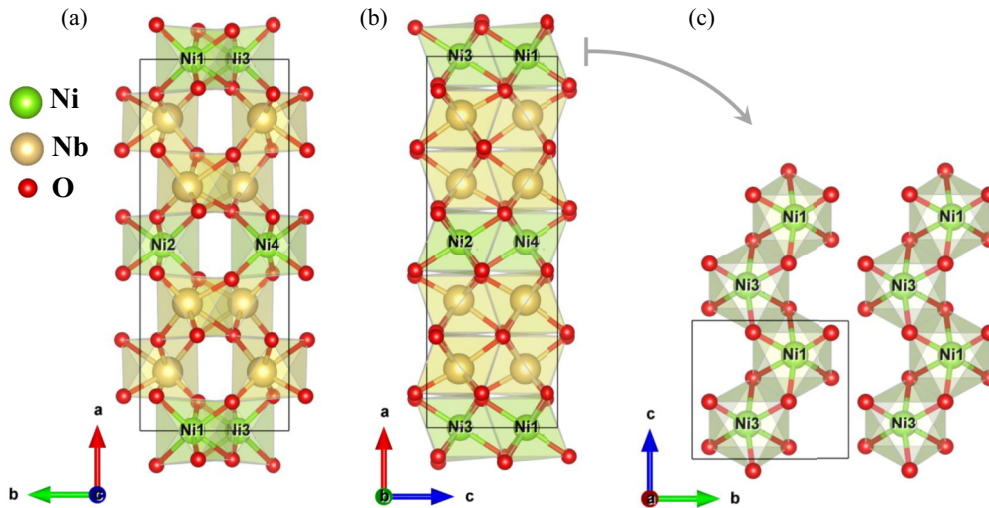*s.singh@rochester.edu
†subhasht@iitg.ac.in

FIG. 1. A unit cell of NiNb$_2$O$_6$ showing the arrangement of Ni, Nb, and oxygen atoms in (a) the *ab* plane and (b) the *ac* plane. In panel (c), two Ni-Ni ferromagnetic chains are shown within the *bc* plane running along the *c* axis.

associated exchange constants, it is important to first describe its crystal structure and summarize results from previous magnetic studies. In the niobate columbites ANb$_2$O$_6$ (A = Ca, Mn, Fe, Co, Ni, Cu, Zn, and Mg [11–15]), Nb^{5+} is nonmagnetic with the A site being the only magnetic divalent cation. These niobate columbites crystallize in an orthorhombic crystal structure [Figs. 1(a) and 1(b)] with space group $Pbcn$-D_{2h}^{14}, with an A-site cation occupying 4c Wyckoff position possessing strong single-ion anisotropy and Nb^{+5} ion occupying 8d Wyckoff position in the unit cell [16–18]. The lattice parameters of the orthorhombic NiNb$_2$O$_6$ unit cell are $a = 14.0229$ Å, $b = 5.6769$ Å, and $c = 5.0184$ Å [19]. In this orthorhombic-columbite crystal structure, both the NiO$_6$ and NbO$_6$ octahedra form an edge-sharing independent zigzag chains along the c axis [Figs. 1(c) and 11(a)], where the magnetic Ni^{+2} ions are arranged ferromagnetically in NiO$_6$ zigzag chains with superexchange interaction mediated by oxygen ions (Ni-O-Ni). Further, a unique alternate arrangement -Ni-Nb-Nb-Ni-Nb-Nb-Ni- of NiO$_6$ and NbO$_6$ octahedra is present along the a axis. The nearest- and next-nearest Ni^{+2} zigzag chains couple antiferromagnetically, which leads to the formation of an isosceles triangular arrangement of Ni^{+2} ions in the ab plane [Fig. 11(b)]. The noncollinear magnetic moments of Ni^{+2} ions are canted at an angle of 31° to the c axis in the ac plane [19–24]. Furthermore, the spin orientation follows the alignment of NiO$_6$ oxygen octahedra [20].

The first studies of the magnetic properties of NiNb$_2$O$_6$ were reported by Yaeger *et al.* [25] in 1977. From the susceptibility measurements on single crystals, they reported $T_{\mathrm{N}} = 6.0 \pm 0.3$ K. Further, assuming the two-sublattice model in the mean-field approximation for Ni^{+2} ions, Yaeger *et al.* theoretically estimated the anisotropy constant $K = 7.9 \pm 0.7$ K/spin and the anisotropy field $H_{\mathrm{K}} = (98.0 \pm 12.7)$ kOe at $T = 0$ K. Also, the critical fields $H_{\mathrm{a}} = 32.8 \pm 5.6$ kOe, $H_{\mathrm{b}} = 45.4 \pm 6.4$ kOe, and $H_{\mathrm{c}} = 15.1 \pm 10.5$ kOe along the a-, b-, and c-axis were reported. The net dipolar and exchange field, H_{eff} ($= H_{\mathrm{dip}} + H_{\mathrm{E}}$) $= 46.3 \pm 10.5$ kOe and $g = 2.4 \pm 0.1$ were theoretically estimated, but the mean-field approxi-

mation yielded $T_{\mathrm{N}} = 6.5$ K which is slighter greater than the experimental value, $T_{\mathrm{N}} = 6.0$ K. The intrachain ferromagnetic interaction is more prominent compared to interchain antiferromagnetic interaction in NiNb$_2$O$_6$ and this system shows uniaxial magnetocrystalline anisotropy [25].

Temperature-dependent neutron diffraction studies on NiNb$_2$O$_6$ by Heid *et al.* [20] in 1996 reported the existence of antiferromagnetic (AFM) ordering below $T_{\mathrm{N}} = 5.7$ K and showed the existence of two distinct magnetic structures corresponding to the two propagation vectors (0 $^1/_2$ 0) and ($^1/_2$ $^1/_2$ 0). Additionally, at $T = 2$ K, the magnetization measurements on NiNb$_2$O$_6$ single crystal yielded critical fields of $H_c = 10.5$ kOe and $H_a = 27.8$ kOe along the c- and a-axis, respectively. Using mean-field approximation, they determined the intrachain ferromagnetic exchange term $J_0/k_{\mathrm{B}} = 9.86$ K (along the c axis) and interchain antiferromagnetic exchange $J_1/k_{\mathrm{B}} = -0.43$ K (along the ab plane) and $J_2/k_{\mathrm{B}} = -1.07$ K (along the b axis). Since the magnitudes of J_1 and J_2 are very small compared to J_0, this leads to the low-dimensional magnetic behavior in NiNb$_2$O$_6$, but not too low as in CoNb$_2$O$_6$ [22]. However, their mean-field calculations considerably overestimated the Néel temperature $T_{\mathrm{N}} = 15.6$ K compared to the experimental value of $T_{\mathrm{N}} = 5.7$ K. The g factor along the three crystallographic axes $g^{xx} = 2.33$, $g^{yy} = 2.35$, and $g^{zz} = 2.36$ shows weaker anisotropy in NiNb$_2$O$_6$ compared to other columbites like FeNb$_2$O$_6$ and CoNb$_2$O$_6$ [20]. The 2021 studies by Peña *et al.* [19] reported $T_{\mathrm{N}} = 5.7$ K for NiNb$_2$O$_6$ and their fit of the magnetic susceptibility data to the Curie-Weiss law for $T > T_{\mathrm{N}}$ yielded $\Theta_{\mathrm{CW}} = 12.5$ K, $C = 1.33$ emu K/mol Oe, and $\mu_{\mathrm{eff}} = 3.29\,\mu_{\mathrm{B}}$ per Ni^{2+}. In addition, Peña *et al.* reported the ferromagnetic intrachain interaction term $J_0/k_{\mathrm{B}} = 7.12$ K, and the antiferromagnetic interchain interaction term $J_\perp/k_B = -0.29$ K (which is an estimated average of J_1 and J_2 as defined by Heid *et al.* [20]) from the one-dimensional Ising model approximation, and mean-field approximation, respectively [19].

In this paper, we have combined first-principles density-functional theory (DFT) calculations with experiments to

elucidate the magnetic structure of $NiNb_2O_6$. Our calculations correctly describe the magnetic ground state of $NiNb_2O_6$ and reveal the presence of a competing next-neighbor antiferromagnetic exchange interaction within the ferromagnetic Ising chains of Ni. This next-neighbor antiferromagnetic intrachain interaction $J_0^{(2)}$ is about 20% of the magnitude of the nearest-neighbor ferromagnetic intrachain interaction $J_0^{(1)}$ and is responsible for the canting of the Ni^{2+} moments in the *ac* plane. Results from our detailed magnetization measurements covering the temperature (T) range of 1.8 to 300 K in magnetic fields (H) up to 90 kOe are used for complete mapping of the H-T phase diagram along with the determination of the triple point and magnetic exchange constants. In addition, we report measurements of the temperature dependence of heat capacity of $NiNb_2O_6$ from 2 to 35 K and evaluate its critical exponents using the data recorded near $T_N = 5.59$ K. A comprehensive discussion on the comparison of the exchange constants determined here *vis-à-vis* those reported in previous publications is also presented.

This paper is organized as follows: Section II contains the experimental and theoretical details, Sec. III summarizes the specific-heat data, Sec. IV is devoted to the detailed discussion of the magnetic properties, Sec. V presents determination of exchange constants from magnetic data, Sec. VI provides results from the DFT + U calculations, and Sec. VII presents a summary of the main results and conclusions.

II. METHODS

A. Synthesis, experimental methods, and electronic structure of $NiNb_2O_6$

The polycrystalline nickel niobate $NiNb_2O_6$ was synthesized in bulk form by employing the standard solid-state reaction method with the help of a FRITSH ball-milling machine. Initially, the stoichiometric proportion of transition-metal oxides NiO and Nb_2O_5 were weighed accurately and transferred into a tungsten-carbide jar. Next, the 1:5 weight ratio of weighed powder to the tungsten-carbide balls (10-mm diameter) was maintained in the jar, and enough ethanol was used as a milling medium to reduce the friction while milling. Finally, these metal oxide powders were milled homogeneously in a ball-milling machine at a speed of 120 rpm for 12 h. The milled aqueous solution was dried in an oven for 24 h before being pressed into cylindrical pellets with a hydraulic press at a pressure of $50 \, kg \, cm^{-2}$. The cylindrical pellets were sintered at 1200 °C for 36 h in air. To increase the crystallinity, the first sintered pellets were remilled and resintered at 1250 °C for 48 h in air.

The crystal structure and phase purity of this bulk polycrystalline $NiNb_2O_6$ sample were investigated using a Bruker x-ray diffractometer (model: D8 ADVANCE ECO) with a Cu-Kα ($\lambda = 1.5406$ Å) source. The recorded x-ray-diffraction pattern of $NiNb_2O_6$ at room temperature was refined by using Rietveld FULLPROF suite software (see Fig. 2), which yields the lattice parameters $a = 14.0374(1)$, $b = 5.6839(2)$, and $c = 5.0245(1)$ Å with $R_{Bragg} = 4.0\%$ and global $\chi^2 = 6.2$. Moreover, these parameters confirm the columbite crystal structure of space group $Pbcn$-D_{2h}^{14} with the absence of secondary phases. The chemical composition and electronic

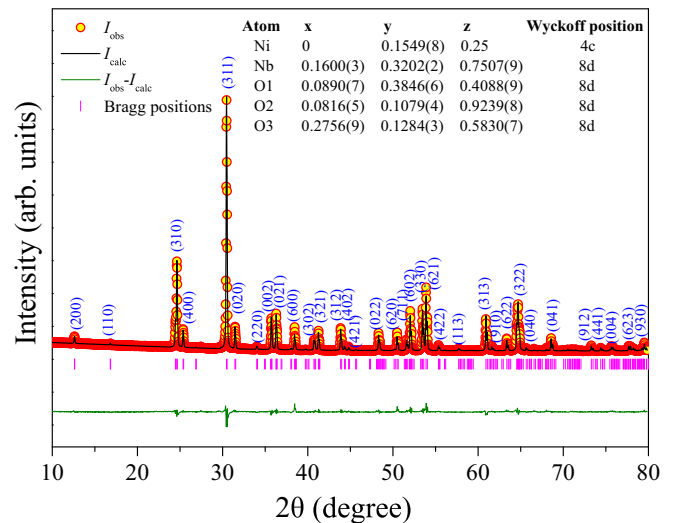| Atom	x	y	z	Wyckoff position
Ni	0	0.1549(8)	0.25	4c
Nb	0.1600(3)	0.3202(2)	0.7507(9)	8d
O1	0.0890(7)	0.3846(6)	0.4088(9)	8d
O2	0.0816(5)	0.1079(4)	0.9239(8)	8d
O3	0.2756(9)	0.1284(3)	0.5830(7)	8d

FIG. 2. Rietveld refined data of room-temperature x-ray-diffraction (XRD) pattern of the $NiNb_2O_6$ sample along with the marked Bragg positions. The bottom green line represents the difference between experimental and simulated XRD pattern. In the inset, coordinates and Wykoff positions of the atoms are listed.

structure of the sample were probed using an x-ray photoelectron spectrometer (XPS) from ULVAC-PHI, Inc. (model: PHI 5000 VersaProbe III) configured with a monochromatic Ag x-ray source with a 20-µm x-ray beam size of 4.5 W. The main conclusion of the results from the XPS analysis, details of which are given in the Supplemental Material, Fig. S1, is the presence of Ni^{+2} and Nb^{+5} states in the polycrystalline $NiNb_2O_6$ sample [26].

The DC magnetic measurements of the sample were carried out using a Physical Property Measurement System (PPMS-DynaCool) in vibrating sample magnetometer mode from Quantum Design, which has a magnetic field strength up to ±9 T and a temperature range of 1.9–400 K. On the other hand, M-H at 1.8 K was measured in a PPMS (CFMS system) from Cryogenic Limited, which has a ±14 T magnet and can operate in the temperature range of 1.8 to 400 K. The heat-capacity measurements of the sample were recorded from 2.5 to 35 K by using the standard heat-pulse calorimetry in the PPMS of Quantum Design. A dual-slope analysis was implemented near the transition temperature to observe the magnetic field effect on phase transition.

B. Computational details

To gain a deeper understanding of the magnetic structure of $NiNb_2O_6$, we conducted first-principles density-functional theory (DFT + U) studies utilizing the projector augmented-wave (PAW) method within the VASP software [27–29]. Eleven, ten, and six valence electrons were considered in the PAW pseudopotentials of Nb, Ni, and O, respectively. The exchange-correlation functional was computed using the generalized-gradient approximation as parametrized by Perdew-Burke-Ernzerhof for solids [30]. The reciprocal space of the primitive unit cell was sampled using a Monkhorst-Pack k mesh [31] of size $3 \times 9 \times 9$. The kinetic energy cutoff for the plane-wave basis set was set to 600 eV. The energy
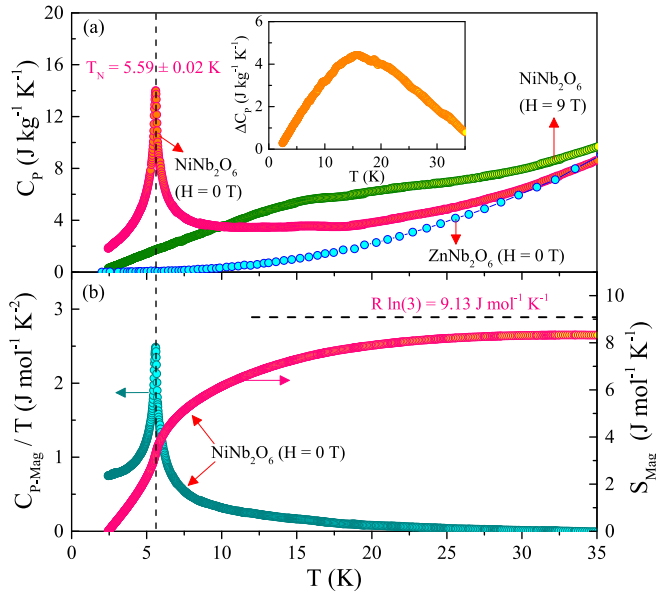
FIG. 3. (a) Temperature dependence of heat capacity C_P (T) data measured at $H = 0$ and $H = 90$ kOe for the NiNb$_2$O$_6$ sample along with the specific-heat data of ZnNb$_2$O$_6$ from Ref. [33]. The inset shows the temperature dependence of the specific-heat difference $\Delta C_P = [C_P(\text{NiNb}_2\text{O}_6, H = 9T) - C_P(\text{ZnNb}_2\text{O}_6, H = 0)]$ peaking near 15 K. (b) Plot of $C_{P\text{-mag}}/T$ vs T shows the ordering temperature at $T_N = 5.59 \pm 0.02$ K and the plot of entropy S_{mag} vs T (right y scale).

and force convergence criteria in all DFT $+ U$ calculations were set to 10^{-7} eV and 10^{-3} eV/Å, respectively. The on-site Coulomb interaction effects for Ni $3d$ electrons were addressed at the mean-field level using the rotationally invariant DFT $+ U$ method proposed by Liechtenstein *et al.* [32]. We fixed $U = 5.0$ eV and $J = 1.0$ eV for Ni $3d$ orbitals, as this set of values correctly describes the ground-state magnetic ordering and accurately predicts the lattice parameters within $\sim 0.2\%$ uncertainty compared to the experimental data. To determine the first- and second-neighbor magnetic exchange interactions, we performed DFT $+ U$ calculations on a $1 \times 2 \times 2$ supercell considering the collinear magnetic configurations, i.e., no spin-orbit coupling effects were considered. The DFT $+ U$ optimized lattice parameters for the antiferromagnetic ground state (discussed below) in *Pbcn* crystallographic space group are $a = 14.0751$, $b = 5.6837$, and $c = 5.0144$ Å, which are in good agreement with our experimental data.

III. THERMAL VARIATION OF SPECIFIC HEAT AND CRITICAL EXPONENTS NEAR NÉEL TEMPERATURE

The measurements of specific heat C_P (T) vs T carried out in the temperature range of 2.5 to 35 K for $H = 0$ and $H = 90$ kOe are shown in Fig. 3(a). The zero-field C_P curve indicates a clear λ-type anomaly across the transition temperature, $T_N = 5.59 \pm 0.02$ K. But, the C_P vs T data at $H = 90$ kOe do not show any sharp peak; instead, C_P increases gradually with increasing temperature up to 35 K. For $H = 90$ kOe, the system is in a forced ferromagnetic state as shown later (see Fig. 8) and so

the anomaly in C_P observed for $H = 0$ at T_N is not observed for $H = 90$ kOe since the system is already in ordered state. This also explains why C_P ($H = 90$ kOe)$< C_P$ ($H = 0$) for $T < 10$ K. However, for $T > 10$ K, the observation that C_P ($H = 90$kOe) $> C_P(H = 0)$ may be due to extra contribution from magnons present in the forced ferromagnetic state. In the inset of Fig. 3(a), plot of the temperature dependence of the specific-heat difference $\Delta C_P = [C_P(\text{NiNb}_2\text{O}_6, H = 9T) - C_P(\text{ZnNb}_2\text{O}_6, H = 0)]$ shows a peak near 15 K. This peak may be related to the fact that in temperature units ($k_B T = g\mu_B H$), 1 T $= 10^4$ Oe ~ 1.57 K using $g = 2.33$ determined later for NiNb$_2$O$_6$, and so 9T ~ 14 K. Therefore, above $T = 14$ K corresponding to $H = 9$ T, thermal energy is large enough to reduce the contributions from magnons yielding the observed peak for ΔC_P. The C_P (T) measurements of isostructural nonmagnetic ZnNb$_2$O$_6$ system [33] are utilized here and below to determine this magnetic contribution to C_P.

In antiferromagnets, the magnetic contribution to specific heat varies as T^3, which is the same as the lattice contribution at lower temperatures. This same temperature dependence leads to difficulty in the separation of magnetic and lattice specific heats. Again, we utilized the C_P (T) measurements of isostructural nonmagnetic ZnNb$_2$O$_6$ system [33] to determine the $C_{P\text{-mag}}$ vs T for the $H = 0$ case.

In Fig. 3(b), the magnetic specific heat is plotted as $C_{P\text{-mag}}/T$ vs T for $H = 0$; the sharp λ-type anomaly indicates the long-range magnetic ordering below $T_N = 5.59$ K. The magnetic entropy, S_{mag}, of magnons in spin waves is calculated by numerical integration of $C_{P\text{-mag}}/T$ by using Eq. (1) listed below [34], which is shown in the right y scale of Fig. 3(b) for the temperature range of 2.5 to 35 K at $H = 0$. Beyond $T = 33$ K, the total S_{mag} saturates at 8.33 J mol^{-1} K^{-1} for zero field. Moreover, the S_{mag} saturation indicates the domination of phonon contribution at $T > 33$ K. The theoretical estimate of $S_{mag} = R\ln(2S + 1)$ for $S = 1$ [34], which possesses three degenerate magnetic ground states, produces the limiting value of $S_{mag} = 9.13$ J mol^{-1} K^{-1}, which is in close agreement with the experimental estimate of $S_{mag} = 8.33$ J mol$^-$ K^{-1} ($\sim 91\%$) at $T = 33$ K for $H = 0$. Using this experimental S_{mag} value and $R = 8.314$ J mol^{-1} K^{-1}, we determined the spin, $S = 0.86 \approx 1$ for the NiNb$_2$O$_6$ system.

$$S_{mag}(T) = \int_0^T \frac{C_{P\text{-mag}}}{T} \, dT. \tag{1}$$

The specific-heat data in Fig. 3(a) display a clear second-order magnetic phase transition at $T_N = 5.59$ K with no latent heat for $H = 0$. Further, to estimate the behavior of C_P in the vicinity of T_N both in the ordered and disordered phase, we employed a critical exponent analysis using the equation $C_P = A(T - T_N)^{-\alpha}$, where α is the critical exponent and A is a constant [35]. The exponent α is determined for both critical regions, $T > T_N$ and $T < T_N$, using the linear fit of the C_P vs $|T - T_N|$ plot represented in log scale as shown in Fig. 4. The ordering temperature T_N is varied in steps of 0.01 K from 5.58 to 5.61 K for the best linear fit and the corresponding α values. We found an excellent fit for $T_N = 5.59$ K with $\alpha = 0.349(1)$ for $T < T_N$ valid in the critical
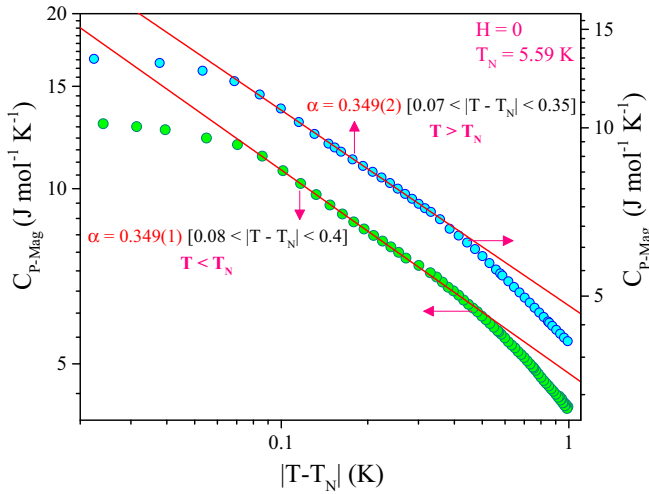
FIG. 4. Thermal variation of $C_{P\text{-Mag}}$ in the vicinity of T_N is fitted to the equation $C_P = A|T - T_N|^{-\alpha}$ using log-log plot with the linear fits yielding exponent α for both $T < T_N$ and $T > T_N$.

region $0.08 < |T - T_N| < 0.40$ and $\alpha = 0.349(2)$ for $T > T_N$ valid in the critical region $0.07 < |T - T_N| < 0.35$ for the NiNb$_2$O$_6$ system using the least-square linear-fit analysis. For comparison, $\alpha \sim 0.05$ has been reported for cubic antiferromagnet RbMnF$_3$ [36], $\alpha = 0.1$ for uniaxial antiferromagnet MnF$_2$ [37], and $\alpha = 0.68$ and $\alpha = 0.58$, respectively, for 3D Ising antiferromagnets CoCs$_3$Cl$_5$ and CoK$_2$(SO$_4$)$_2$ · 6H$_2$O [38]. The magnitude of $\alpha \sim 0.35$ reported here for NiNb$_2$O$_6$ falls in between that observed in uniaxial MnF$_2$ and the 3D Ising systems [38]. These comparisons suggest that magnitude of α increases with increase in magnetic anisotropy.

IV. MAGNETIZATION RESULTS AND DISCUSSION

A. Magnetic ordering temperature and its magnetic field dependence

The temperature (3–300 K) dependence of DC-magnetic susceptibility data, $\chi(= M/H)$ at $H = 500$ Oe in both zero-field cooled (ZFC) and field-cooled (FC) conditions are shown in Fig. 5(a) for the studied NiNb$_2$O$_6$ sample. Initially, the sample was cooled from 300 to 3 K in the presence of $H = 0$ Oe ($H = 500$ Oe) for ZFC (FC) protocol, and the magnetic measurements were recorded during warming of the sample up to 300 K. The plots of χ_{FC} and χ_{ZFC} vs T in Fig. 5(a) for $H = 500$ Oe show that χ_{FC} and χ_{ZFC} are effectively equal in the entire temperature range, both peaking at $T_P = 6.5$ K, followed by rapid decrease with decreasing temperatures. For comparison, the temperature dependence of magnetic susceptibility in single crystals of NiNb$_2$O$_6$ reported by Yaeger *et al.* [25] for applied H along the a, b, and c axes showed that χ_a and χ_b are effectively temperature independent below T_P, but χ_c for H applied along the easy c axis decreases rapidly towards zero with decrease in T below T_P. Comparing the magnitudes of χ_{FC} and χ_{ZFC} in our polycrystalline sample at $T_P = 6.5$ K and at the lowest $T = 3$ K in Fig. 5(a) with those of χ_a, χ_b, and χ_c reported in single crystal of NiNb$_2$O$_6$ [25], it is found that as expected, the measured χ in our polycrystalline sample of NiNb$_2$O$_6$ is effectively an average of χ_a, χ_b,
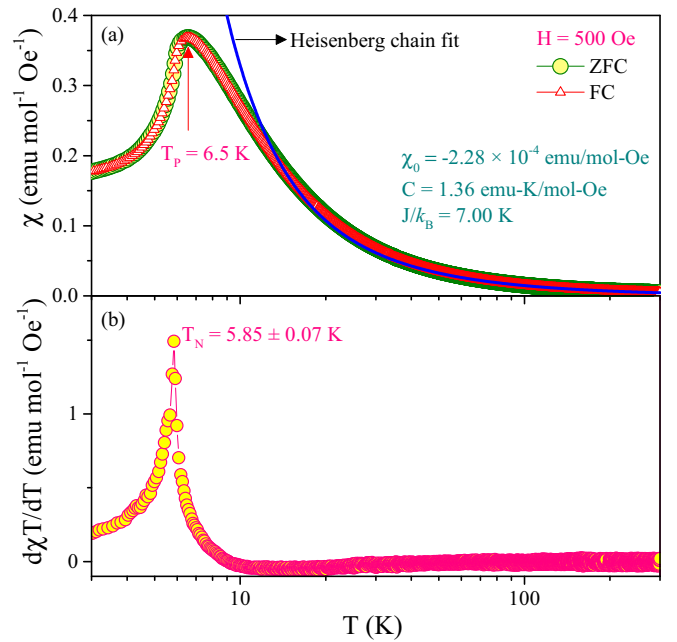

FIG. 5. (a) Temperature dependence of DC-susceptibility χ measured at $H = 500$ Oe showing a broad peak at $T_P = 6.50$ K in both ZFC and FC condition; Fit of χ vs T to the Heisenberg linear chain model [Eq. (5)] is shown as a blue line with the parameters of the fit listed in the figure. (b) Computed plot of $d(\chi T)/dT$ vs T showing a sharp peak corresponding to the AFM to PM phase transition at $T_N = 5.85 \pm 0.07$ K.

and χ_c. Also, the temperature dependences of χ_a, χ_b, and χ_c in NiNb$_2$O$_6$ [25] are similar to those in other antiferromagnets in which $\chi(\parallel)$ measured for H applied along the easy axis rapidly decreases with decrease in $T < T_P$ approaching zero for $T = 0$ K, but $\chi(\perp)$ for H applied perpendicular to the easy axis is nearly temperature independent for $T < T_P$, leading to a positive constant value in the $T = 0$ K limit. In χ vs T variation in Fig 5(a) for our polycrystalline NiNb$_2$O$_6$, the rapid decrease with decrease in $T < T_P$ is interpreted to be due to the $\chi(\parallel)/3$ contribution of rapidly decreasing parallel susceptibility χ_c.

The Néel temperature, T_N, in antiferromagnets is usually less than T_P; instead, T_N is accurately determined by the peak in the $\partial(\chi(\parallel)T)/\partial T$ vs T plot, because the product $[\chi(\parallel).T]$ represents the magnetic energy, and its temperature derivative is equivalent to the heat capacity [39–44]. As noted above, in our polycrystalline NiNb$_2$O$_6$, measured χ contains $\chi(\parallel)/3$ contribution from the parallel susceptibility of χ_c and so in a plot of $\partial(\chi T)/\partial T$ vs T, a peak would be expected because of the contribution from χ_c. The plot of the computed $\partial(\chi T)/\partial T$ vs T in Fig. 5(b) indeed resembles the λ-type anomaly across the transition temperature in specific-heat data. This computed $\partial(\chi T)/\partial T$ vs T plot in Fig. 5(b), yields a peak at $T_N = 5.85 \pm 0.07$ K for $H = 500$ Oe, which is slightly larger than $T_N = 5.59 \pm 0.02$ K determined from heat-capacity analysis at $H = 0$ [Fig. 3(a)]. This small difference may be due to the presence of $\chi(\perp)$ in the measured χ since the temperature dependence of $\chi(\perp)$ for $T < T_P$ is much weaker. For comparison, in NiNb$_2$O$_6$, $T_N = 5.7$ K was reported by Heid *et al.*
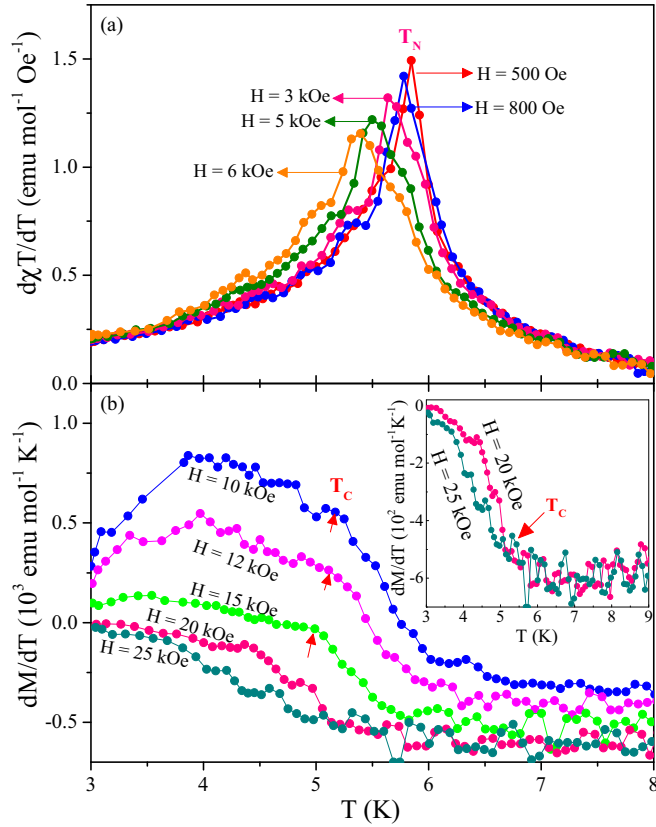
FIG. 6. Plots of (a) $d(\chi T)/dT$ vs T and (b) dM/dT vs T using the measured M vs T plots for $H < 10$ kOe and $H > 10$ kOe, respectively. Inset in (b) shows location of T_C for $H = 20$ and 25 kOe.

[20] and Peña *et al.* [19], and $T_N = 6.0 \pm 0.3$ K was reported by Yaeger *et al.* [25]. It is noted that the $\partial(\chi T)/\partial T$ analysis to determine T_N in NiNb$_2$O$_6$ is valid only for $H < 10$ kOe [Fig. 6(a)], since only for $H < 10$ kOe the transition is from a low-temperature AFM state to high-temperature paramagnetic (PM) state. This method fails for $H \geqslant 10$ kOe because the transition then is from a spin-flip phase to the PM phase and the peaks are very broad. Since the spin-flip phase has some AFM component combined with more FM component, the corresponding ordering temperature T_C is determined from the inflection points (marked by arrows) in dM/dT vs T curves up to 15 kOe as shown in Fig. 6(b). Above 15 kOe, since the FM component is more dominant in the spin-flip phase, the minimum in the dM/dT vs T curves is considered as T_C, which is clearly shown in the inset of Fig. 6(b). From overall observation, the ordering temperatures (T_N or T_C) reduces from 5.85 to 5 K as the magnetic field increases from $H = 500$ to 25 kOe. Beyond $H = 25$ kOe the system tends to saturate near $T = 5$ K as noticeable in the H-T phase diagram shown later (see Fig. 10).

B. Temperature dependence of DC-magnetic susceptibility

The thermal dependence of paramagnetic susceptibility χ for $T > T_N$, has been analyzed through the mathematical curve-fitting approach of modified Curie-Weiss (MCW)
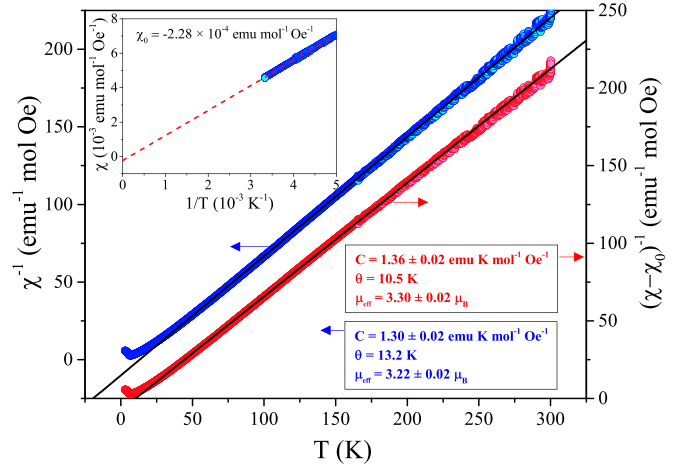

FIG. 7. Temperature dependence of inverse magnetic susceptibility $(\chi - \chi_0)^{-1}$ for $\chi_0 = 0$ and -2.28×10^{-4} emu mol^{-1} Oe^{-1} in left- and right y scale, respectively. Note that the y scales for the two plots are different and shifted. The solid black lines represent the linear fits to MCW [Eq. (2)] in the paramagnetic region yielding the magnitude of C and θ listed in the figure. Plot of χ vs $1/T$ is shown in the inset for the estimation of χ_0 through linear extrapolation of χ in the limit $1/T \to 0$ from high-temperature data points.

law [45]:

$$\chi = \chi_0 + \frac{C}{(T - \theta)}. \tag{2}$$

Here, the magnitude of χ_0 is negligible and it is a temperature-independent term which arises due to the diamagnetic contribution of materials, and also from the Van Vleck susceptibility if present. The experimental estimate of χ_0 is very challenging due to its negligible value; for this purpose we plotted χ vs $1/T$ (inset of Fig. 7) with the linear extrapolation of χ for $1/T \to 0$ yielding $\chi_0 = -2.28 \times 10^{-4}$ emu mol^{-1} Oe^{-1}, where the paramagnetic term $C/(T - \theta)$ in Eq. (2) vanishes. Using $\chi_0 = -2.28 \times 10^{-4}$ emu mol^{-1} Oe^{-1} and $\chi_0 = 0$, we have plotted $(\chi - \chi_0)^{-1}$ vs T as shown in the right- and left y scales of Fig. 7, respectively. The linear fit to the plot $(\chi - \chi_0)^{-1}$ vs T in the higher-temperature region ($T > 30$ K) yields $C = 1.36 \pm 0.02$ emu K mol^{-1} Oe^{-1} and $\theta = 10.5$ K for $\chi_0 = -2.28 \times 10^{-4}$ emu mol^{-1} Oe^{-1}, whereas $C = 1.30 \pm 0.02$ emu K mol^{-1} Oe^{-1} and $\theta = 13.2$ K are obtained for $\chi_0 = 0$. The positive value of θ suggests that the dominant exchange interaction is ferromagnetic in NiNb$_2$O$_6$, which is consistent with our theoretical investigations, details of which are presented later.

The equation $C = N_A \mu_{\text{eff}}^2 / 3k_B$ (N_A = Avogadro's number, k_B = Boltzmann constant) yields the effective magnetic moment $\mu_{\text{eff}} = 3.30(2) \mu_B$/Ni^{2+} for $\chi_0 = -2.28 \times 10^{-4}$ emu mol^{-1} Oe^{-1} and $\mu_{\text{eff}} = 3.22(2) \mu_B$/Ni^{2+} for $\chi_0 = 0$. Previous studies by Peña *et al.* [19] and Sarvezuk *et al.* [45], respectively, reported $\mu_{\text{eff}} = 3.29 \mu_B$ and $\mu_{\text{eff}} = 3.3 \mu_B$ per Ni^{2+} ion, which are in excellent agreement with our result, $\mu_{\text{eff}} = 3.30(2) \mu_B$/Ni^{2+} for $\chi_0 \neq 0$. Thus, the correction for χ_0 is important since it leads to more accurate determination of μ_{eff}, C, and θ values.
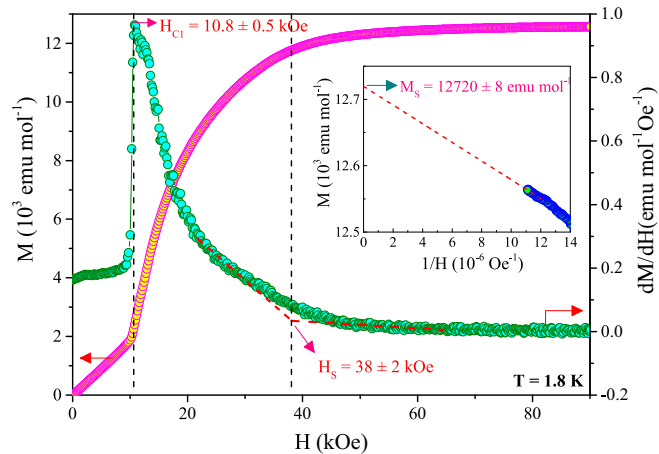
FIG. 8. Magnetic field dependence of magnetization (M) at 1.8 K and the corresponding plot of computed dM/dH vs H in the right y scale peaks at $H_{C1} = 10.8 \pm 0.5$ kOe. The dashed red lines show the linear extrapolation of dM/dH for the determination of $H_S = 38 \pm 2$ kOe. The plot of M vs $1/H$ at $T = 1.8$ K is shown in the inset for the estimation of M_S in the limit of $1/H \to 0$ using the data for $H > 40$ kOe.

The g factor is determined from the equation $\mu^2 = g^2 \mu_B^2 S(S + 1)$ and by using $\mu_{eff} = 3.30(2)\,\mu_B/\text{Ni}^{2+}$ (obtained from MCW law) with $S = 1$ yields $g = 2.3334$, which is in very good agreement with g (average of g^{xx}, g^{yy}, and g^{zz}) = 2.34 reported by Heid et al. [20]. Since $g > 2$, it signifies some contribution of spin-orbit coupling effect to the magnetic ground state of Ni^{2+}. The z component of effective magnetic moment $\mu_z = gS\,\mu_B$ is estimated using $g = 2.3334$

(for $\chi_0 \neq 0$) and $S = 1$, which yields $\mu_z = 2.33\,\mu_B$, in good agreement with $\mu_z = 2.4\,\mu_B$ reported by neutron-diffraction analysis of Heid et al. [20].

C. Magnetic field-induced spin-flip transitions and saturation magnetization

The magnetic field dependence of magnetization $M(H)$ was measured at 1.8 K from 0 to 90 kOe for the polycrystalline NiNb_2O_6 sample, which shows a noticeable slope change near 10.8 kOe as displayed in Fig. 8. Similar M vs H measurements have been carried out up to 90 kOe for the temperatures below T_N, and the slope change at various temperatures can be noticed in the inset of Fig. 9 up to 14 kOe. Further, the critical field corresponding to slope change can be accurately determined by $\partial M/\partial H$ vs H plot, which yields a peak at $H_{C1} = 10.8$ kOe for $T = 1.8$ K as shown in the right y scale of Fig. 8. This value is in excellent agreement with $H_c = 10.5$ kOe for $H \| c$ at $T = 2$ K reported in single crystals by Heid et al. [20], and in concordance with our estimated value of $H_{C1} = 10.6$ kOe at $T = 1.7$ K from the digitalized data of Peña et al. [19]. Similarly, for different $T < T_N$, the $\partial M/\partial H$ vs H plots are shown in Fig. 9, showing a decreasing trend of H_{C1} with increasing temperature.

In NiNb_2O_6, the Ni^{2+} ferromagnetic chains along the c axis align antiferromagnetically with the neighbouring chains resulting in an overall antiferromagnetic ordering. For $H > H_{C1}$, fraction of grains whose local easy axis (c axis) coincides with the direction of applied field flip the spins of oppositely oriented neighboring ferromagnetic chains to align along its direction. This leads to a transition from AFM to spin-flip phase as shown in the latter H-T phase diagram (Fig. 10).
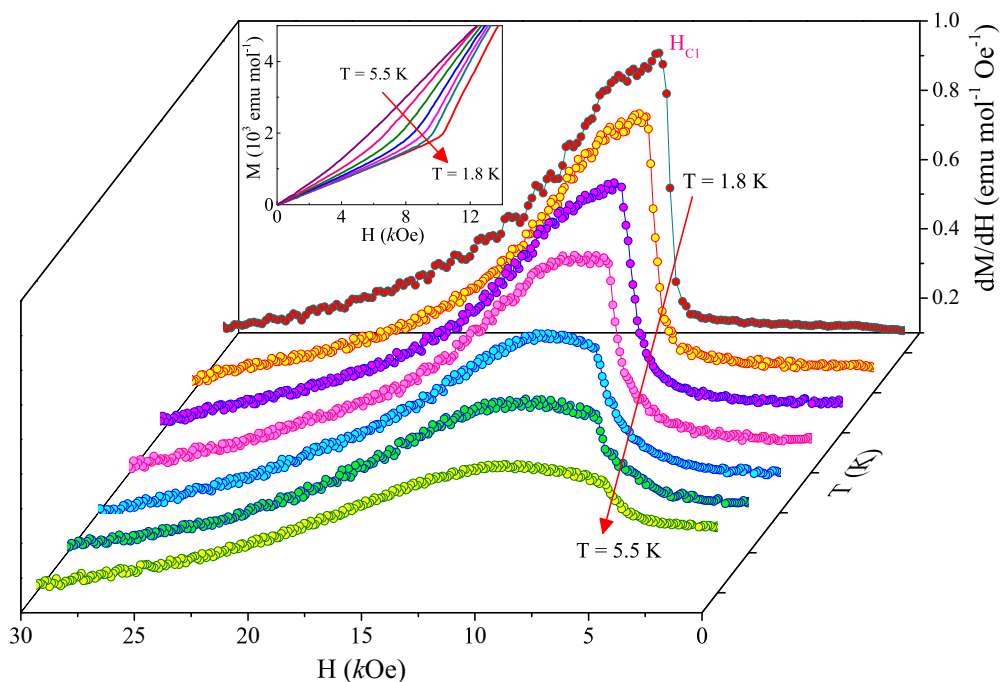

FIG. 9. Plots of computed dM/dH vs H using the data of isothermal M vs H curves for various temperatures (1.8 to 5.5 K) with the peaks yielding spin-flip field, H_{C1}. Inset shows the clear change of slopes near H_{C1} in M vs H plots at different T.
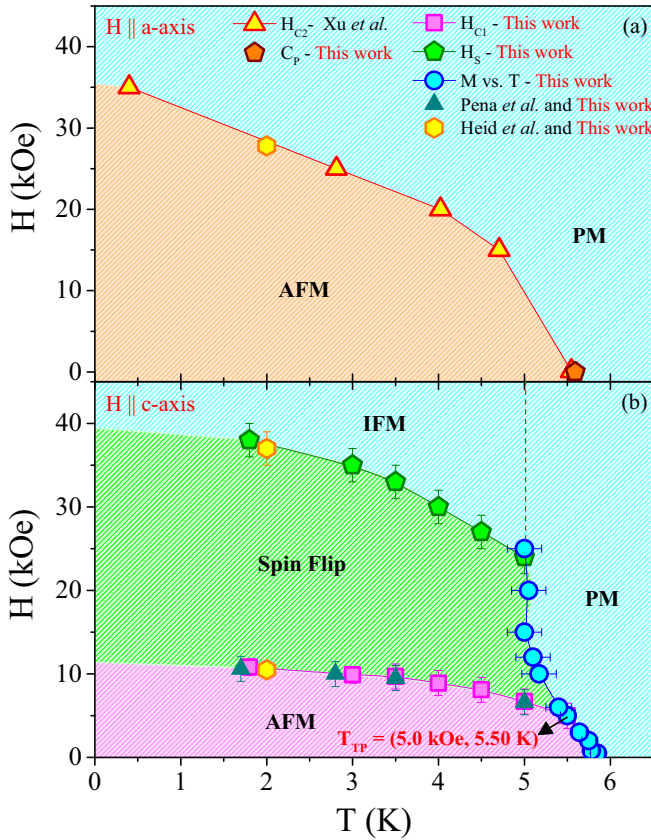
FIG. 10. *H*-*T* phase diagram of NiNb$_2$O$_6$ sample for *H* parallel to the *a* axis in (a) and *H* parallel to the *c* axis yielding a triple point, $T_{\text{TP}}(H, T) = (5 \text{ kOe}, 5.50 \text{ K})$ in (b). Lines connecting the data points are visual guides, and references to sources of the data points are listed in the figure. The acronyms used for the magnetic phases are as follows: PM, paramagnetic; AFM, antiferromagnetic; and IFM, induced ferromagnetic.

Usually spin-flip transitions are first order with a finite jump in magnetization and possess hysteresis loops, which are observed in NiNb$_2$O$_6$ single crystal [20]. However, the current sample being polycrystalline, we observe a continuous change in magnetization, although Sarvezuk *et al.* [46] reported a weak hysteresis loop even in a powder sample. Since the *a* axis is an intermediate hard axis, as *H* exceeds H_{C2} some fraction of grains have their *a* axis aligning with the external field direction, which would yield another spin-flip phase transition. The critical field H_{C2} could not be detected for the current polycrystalline sample, likely because fewer grains are oriented along the field direction, but $H_{\text{C2}} = H_a = 27.8$ kOe for $H \parallel a$ is reported in single-crystal studies [20]. Further increase in *H* at a specific field $H_{\text{S}}(= M_{\text{S}}/\chi_{\perp})$ leads to the induced ferromagnetic state (IFM), where all the spins are forcibly brought to align parallel to the applied field by overcoming the exchange-coupling field, H_{E} ($= H_{\text{S}}$). The magnetic field $H_{\text{S}} = 38 \pm 2$ kOe at $T = 1.8$ K is determined from the linear extrapolation of $\partial M/\partial H$ vs *H* curve, which is shown as dotted lines in Fig. 8 [43]. Since the *b* axis is the hardest axis, hence this experimental value is in close agreement with our estimated value $H_b = 37 \pm 2$ kOe for $H \parallel b$ axis at $T = 2$ K from the digitalized data of Heid

et al. [20]. Similar estimation of H_{S} has been done for different temperatures up to 5 K, above which the system enters the paramagnetic region as shown in the *H*-*T* phase diagram (Fig. 10).

The saturation magnetization is determined from the *M* vs $1/H$ plot at 1.8 K as shown in the inset of Fig. 8; the linear extrapolation of *M* in the limit of $1/H \to 0$ yields $M_{\text{S}} = 12720(8)$ emu mol^{-1}. Further, using the relation $M_{\text{S}} = N_A g \mu_B S$ at absolute zero and $g = 2.3334$ (obtained from MCW law) with $S = 1$ yields the calculated $M_{\text{S}} = 13032$ emu mol^{-1}. This calculated value is just 2.4% larger than the experimental value, and this minute difference is attributed to the decreasing nature of M_{S} with increasing temperature, as we estimated M_{S} experimentally at 1.8 K compared to the calculated value at 0 K. This good agreement confirms the spin $S = 1$ and $g = 2.3334$ for the magnetic ground state of Ni^{+2} in NiNb$_2$O$_6$ sample. Next, from $H_{\text{E}} = H_{\text{S}} = 38$ kOe and $M_{\text{S}} = 12720$ emu mol^{-1}, the equation $M_{\text{S}} = \chi(\perp)H_{\text{E}}$ [47] yields $\chi(\perp) = 0.34$ emu mol^{-1} Oe^{-1}, which is in excellent agreement with the peak value of $\chi = 0.36$ emu mol^{-1} Oe^{-1} at $T_{\text{P}} = 6.5$ K measured for $H = 500$ Oe [Fig. 5(a)]. Here, $\chi(\perp)$ is the susceptibility measured perpendicular to the easy axis in single crystals, which is only weakly dependent on temperature below T_{N} and so it is nearly equal to the peak value of χ in AFM systems, similar to the observations in NiNb$_2$O$_6$ [25]. This consistency between experimental and calculated $\chi(\perp)$ provides the confirmation of H_{S} in this columbite.

D. Magnetic field-temperature (H-T) phase diagram and triple point

The magnetic field-temperature (*H*-*T*) phase diagram for $H \parallel a$ and $H \parallel c$ axes is shown in Figs. 10(a) and 10(b), respectively. For the $H \parallel a$ axis, we utilized the temperature dependence of C_{P} data at various magnetic fields measured on single crystal from Ref. [8], where the T_{N} reduces almost to zero as *H* approaches the critical field, $H_{\text{QCP}} \sim 35$ kOe. Further increase of H > 35 kOe near 0 K results in growth of quantum fluctuations and leads to quantum disorder phase. Next, we included the spin-flip field H_a for the $H \parallel a$ axis from Ref. [20] and $T_{\text{N}} = 5.59 \pm 0.02$ K from the current C_{P} data at $H = 0$ in Fig. 10(a).

Since H_{C1} falls in the range of H_c for $H \parallel c$ on single crystal (from Ref. [20]), we used the temperature variation of H_{C1} and H_{S} determined from $\partial M/\partial H$ vs *H* plots for the mapping of *H*-*T* phase diagram along the $H \parallel c$ axis [Fig. 10(b)]. Further, we included T_{N} vs *H* and T_{C} vs *H* from the peaks and inflection points in $\partial(\chi T)/\partial T$ vs *T* and $\partial M/\partial T$ vs *T* plots, respectively, at different *H*. Additionally, we added the magnetic field H_b determined from the digitalized data of Ref. [20] at 2 K which lie in the range of H_{S}. Our estimation of H_{C1} vs *T* from the digitalized *M* vs *H* data of Peña *et al.* [19] at different temperatures follows the same trend as the H_{C1} vs *T* reported for the current sample as shown in Fig. 10(b). Summarizing all the data points leads to four distinct magnetic phases that include AFM, spin-flip, IFM, and PM phase with a triple point at $T_{\text{TP}}(H, T) = (5.0 \text{ kOe}, 5.50 \text{ K})$, where AFM, spin-flip, and PM phases coexist in the *H*-*T* phase diagram mapped along the $H \parallel c$ axis [Fig. 10(b)]. This determination
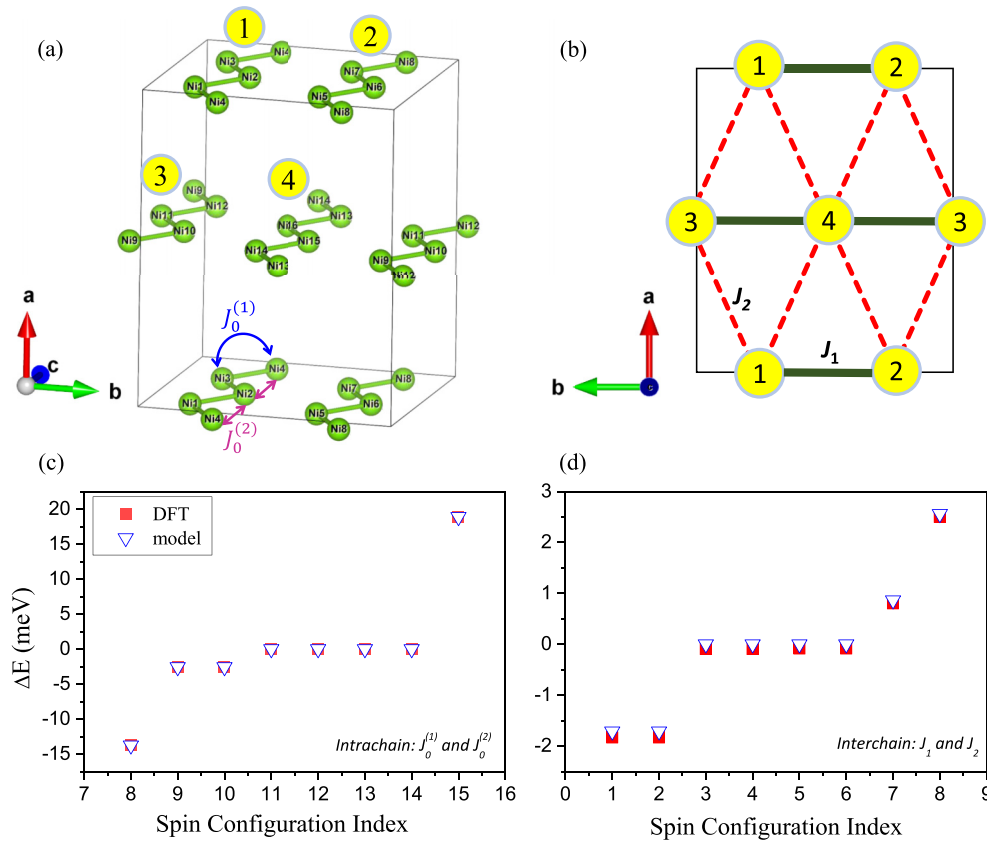
FIG. 11. Schematic diagram of $NiNb_2O_6$ structure which shows only Ni atoms for brevity. (a) represents the zig-zag intrachain of Ni-Ni atoms running along c axis. $J_0^{(1)}$ and $J_0^{(2)}$ denote the first and second NN intrachain interactions within each Ni-Ni chain, respectively. (b) represents the hexagonal-like lattice of Ni-Ni ferromagnetic chains as viewed from the c axis. J_1 and J_2 denote the interchain interaction between the Ni-Ni ferromagnetic chains at the mean- field level. The estimated bond length for $J_0^{(1)}$, $J_0^{(2)}$, J_1, and J_2 exchange interactions is 3.0, 5.0, 4.6, and 7.6 Å, respectively. Fitting of the DFT $+ U$ energy values computed for various different collinear spin configurations in a $1 \times 2 \times 2$ supercell, with our Hamiltonian for the (c) intrachain and (d) interchain spin models.

of the H-T phase diagram for $NiNb_2O_6$ system is a significant result of this work.

V. MAGNETIC STRUCTURE AND EXCHANGE CONSTANTS

Since $NiNb_2O_6$ possesses similar crystal structure and similar magnetic moment alignment with tilt angle $31°$ to the c axis as the $CoNb_2O_6$ system, it exhibits similar intrachain ferromagnetic exchange interactions (J_0) along the c axis and the interchain antiferromagnetic exchange interactions with constants J_1 and J_2 along the b axis and in the ab plane, respectively [Figs. 11(a) and 11(b)]. To evaluate the exchange constants for the present system, we used the same method as in the $CoNb_2O_6$ system reported in Ref. [48]. For this we solved the equations of energy eigenvalues from the proposed Hamiltonian in Ref. [48] and obtained the following equations for J_1 and J_2:

$$J_1 = -g\mu_B \cos\alpha(2H_{C1} + H_S)/(6S), \quad (3)$$

and

$$J_2 = -g\,\mu_B \cos\alpha\,(H_S - H_{C1})/(6S\cos 2\alpha). \quad (4)$$

Using the experimental values of $H_{C1} = 10.8$ kOe and $H_S = 38$ kOe for $H\|c$ axis along with $S = 1$, $\alpha = 31°$, and $g = 2.3334$ (obtained from MCW law), Eqs. (3) and (4) yield $J_1/k_B = -1.335$ K and $J_2/k_B = -1.298$ K, respectively. The slightly higher magnitude of J_1 compared to J_2 indicates relatively stronger AFM interactions along the b axis, which is due to the relatively shorter bond distance along the b axis (5.68 Å) compared to the longer bond distance along the diagonal (7.57 Å) in the ab plane.

Next, by using the standard equation $J_0/k_B = 3T_C/[ZS(S + 1)]$ from the molecular-field theory with $S = 1$, $T_C = 5.60$ K (near the triple point, T_{TP} above which the spin-flip to PM transition occurs) and $Z = 2$ (nearest neighbors along the ferromagnetic chain, i.e., c axis) yields $J_0/k_B = 4.20$ K. The above estimated results are listed in Table I along with the exchange constants reported in the previous works [19,20,46].

The temperature variation of magnetic susceptibility for the Heisenberg linear chain (HLC) is given by [49]

$$\chi = \chi_0 + \frac{C}{T}\left(\frac{1 + \Gamma}{1 - \Gamma}\right). \quad (5)$$

TABLE I. The intrachain ferromagnetic exchange constant, J_0, and the interchain antiferromagnetic exchange constants J_1 and J_2 are listed from this work, Supplemental Material [26] and literature.

J_0/k_B (K)	J_1/k_B	J_2/k_B	Type of spin chain along the c axis	References
4.20	-1.335 K	-1.298 K	Heisenberg	This work
6.01	-0.29 K ($J_\perp$)	-0.29 K ($J_\perp$)	Ising	This work [26]
9.86	-1.07 K	-0.43 K	Heisenberg	[20]
6.0	-0.35 K ($J_\perp$)	-0.35 K ($J_\perp$)	Ising	[46]
7.12	-0.29 K ($J_\perp$)	-0.29 K ($J_\perp$)	Ising	[19]

In Eq. (5), $\Gamma = \coth(y) - (1/y)$ with $y = 2JS^2/k_B T$ and we use $S = 1$, $\chi_0 = -2.28 \times 10^{-4}$ emu mol^{-1} Oe^{-1} and $C = 1.36 \pm 0.02$ emu K mol^{-1} Oe^{-1} obtained from MCW. In Fig. 5(a), the fit of the χ vs T data of NiNb$_2$O$_6$ to Eq. (5) shows excellent fit of the data in the paramagnetic region above 15 K yielding the total magnetic exchange strength, $J/k_B = 7.00$ K. Note that $J/k_B = J_0/k_B + |J_1/k_B| + |J_2/k_B| = 6.833$ K, which is in decent agreement with $J/k_B = 7.00$ K determined from the HLC model. This establishes the accurate determination of exchange constants J_0, J_1, and J_2 in NiNb$_2$O$_6$.

VI. DFT + U CALCULATIONS

To further elucidate the nature of the magnetic exchange interactions in NiNb$_2$O$_6$, we performed first-principles DFT + U calculations as described in Sec. II, Methods. Using the DFT + U optimized primitive cell, we created a $1 \times 2 \times 2$ supercell structure, i.e., 16 formula units of NiNb$_2$O$_6$ containing 4 chains of Ni-Ni atoms running along the c-axis, as shown in Fig. 11(a). We systematically calculated the total energy for all possible collinear spin configurations within the supercell (see Supplemental Table S1 [26]) and mapped the DFT+U calculated total energies onto the spin Hamiltonian given below [50–52].

$$ H = E_0 - J_0^{(1)} \underbrace{\sum_{\langle ij \rangle}^{\text{first NN}} S_i S_j - J_0^{(2)} \sum_{\langle ij \rangle}^{\text{second NN}} S_i S_j}_{\text{Intrachain}} - J_1 \underbrace{\sum_{\langle ij \rangle}^{\text{first NN}} S_i S_j - J_2 \sum_{\langle ij \rangle}^{\text{second NN}} S_i S_j}_{\text{Interchain}} . \tag{6} $$

Here, E_0 represents a rigid shift in total energy, and S_i and S_j denote the spin ordering at different Ni sites. We used four exchange-interaction parameters which can be separated into two parts (see Fig. 11): intrachain ($J_0^{(1)}$ and $J_0^{(2)}$) and interchain (J_1 and J_2). The intrachain $J_0^{(1)}$ and $J_0^{(2)}$ exchange interactions correspond to the first- and second nearest-neighbor (NN) interactions within a Ni-Ni chain, respectively. The interchain J_1 and J_2 exchanges correspond to the first- (// to the b axis) and second-NN (within the ab plane) interactions between the ferromagnetic chains of Ni. Note, in order to estimate J_1 and J_2 at the mean-field level, we consider each Ni-Ni ferromagnetic chain as one spin entity. The corresponding bond distances for the considered intrachain $J_0^{(1)}$ and $J_0^{(2)}$ interactions are 3 and 5 Å, whereas for the interchain J_1 and J_2 interactions are 4.6 and 7.6 Å, respectively.

Figures 11(c) and 11(d) show the fitting of the DFT + U energies ($\Delta E = E - E_0$) computed for different spin configurations without considering spin-orbit coupling effects and the corresponding fitting to our spin Hamiltonian for the intrachain [Fig. 11(c)] and interchain [Fig. 11(d)] interactions. The best fit of the data yields intrachain $J_0^{(1)} S^2 = +1.02$ meV, $J_0^{(2)} S^2 = -0.2$ meV, and interchain $J_1 S^2 = -0.4$ meV, $J_2 S^2 = -0.11$ meV. The positive (negative) sign denotes FM (AFM) magnetic interactions. Considering $S = 1$, we obtain $J_0^{(1)}/k_B = +11.8$ K, $J_0^{(2)}/k_B = -2.32$ K, $J_1/k_B = -4.64$ K, and $J_2/k_B = -1.28$ K. These results imply that the nearest-neighbor intrachain $J_0^{(1)}$ interaction is responsible

for setting the ferromagnetic order within each Ni-Ni chain. Interestingly, we also notice the presence of a relatively small but significant ($\sim 20\%$ of $|J_0^{(1)}|$) second-NN interchain interaction $J_0^{(2)}$ having an AFM nature [Fig. 11(a)]. We argue that this exchange interaction could play a pivotal role in setting the canted magnetic moments of Ni^{2+} ions in the ac plane, as observed in experiments [20]. The interchain exchange interactions, J_1 and J_2, are both antiferromagnetic in nature ($|J_1| > |J_2|$), with smaller magnitudes compared to the dominant intrachain interaction $J_0^{(1)}$, which are consistent with our experimental observations (see Table I). It is worth noting that our DFT + U calculated exchange parameters are overestimated compared to the experimental results. This is primarily because DFT + U calculations were performed for collinear magnetic configurations without considering spin-orbit coupling effects, i.e., no canting of moments was considered. Furthermore, in our theoretical spin model, we consider two distinct intrachain parameters: the nearest-neighbor $J_0^{(1)}$ and the next-nearest neighbor $J_0^{(2)}$ parameters. This approach allows us to account for the competing second-neighbor AFM intrachain exchange, which is ignored when using just one parameter J_0 in our experiments, as discussed above.

VII. SUMMARY AND CONCLUDING REMARKS

From the comprehensive experimental and theoretical studies reported here on the nature of magnetism in

$NiNb_2O_6$, the following results are highlighted. First, the fit of the paramagnetic susceptibility $\chi(T)$ vs T data to $\chi = \chi_0 + C/(T - \theta)$ with $\chi_0 = -2.28 \times 10^{-4}$ emu mol^{-1} Oe^{-1} yielded positive $\theta = 10.5$ K characteristic of dominant ferromagnetic exchange coupling, and $C = 1.36 \pm 0.02$ emu K mol^{-1}Oe^{-1}, the latter yielding $\mu_{\text{eff}} = 3.30(2)\,\mu_{\text{B}}$ per Ni^{2+} ion with effective $g = 2.3334$. Second, results from the magnetic field-induced transitions reported here along with those from previous studied led to the important H-T phase diagram shown in Fig. 10 for the easy and hard directions including the triple point T_{TP} (H, T) =(5.0 kOe, 5.50 K). Third, fit of the specific heat C_{P} vs T data near T_{N} to $C_{\text{P}} = A|T - T_{\text{N}}|^{-\alpha}$ yielded the critical exponent $\alpha = 0.349(2)$ [0.349(1)] for $T > T_{\text{N}}$ [$T < T_{\text{N}}$] with $T_{\text{N}} = 5.59 \pm 0.02$ K, the latter in close agreement with $T_{\text{N}} = 5.85 \pm 0.07$ K determined from the peak in $\partial(\chi T)/\partial T$ vs T plot. Fourth, using the magnetic data, the intrachain ferromagnetic exchange constant J_0 and the interchain antiferromagnetic exchange constants J_1 and J_2 have been determined (see Table I). Further, the total magnetic exchange interaction strength J obtained from the HLC model confirm the Heisenberg linear chain magnetism of $NiNb_2O_6$. And fifth, the magnetic ground state of $NiNb_2O_6$ determined using DFT + U calculations report the intrachain constants $J_0^{(1)}/k_{\text{B}} = 11.83$ K and $J_0^{(2)}/k_{\text{B}} = -2.32$ K, and interchain constants $J_1/k_{\text{B}} = -4.64$ K and $J_2/k_{\text{B}} = -1.27$ K. However, these exchange constants are somewhat overestimated due to the neglect of spin canting and spin-orbit coupling in the calculations which require more extensive computing power. Additional studies near the triple point may also be quite fruitful.

[1] S. Sachdev, *Quantum Phase Transitions*, 2nd ed. (Cambridge University Press, Cambridge, UK, 2011).

[2] H. V. Löhneysen, A. Rosch, M. Vojta, and P. Wölfle, Rev. Mod. Phys. **79**, 1015 (2007).

[3] Y. Zhou, K. Kanoda, and T-K. Ng, Rev. Mod. Phys. **89**, 025003 (2017).

[4] X. Liu, S. Singh, V. D. Touchette, T. Asaba, J. Brewer, Q. Zhang, Y. Cao, B. Pal, S. Middey, P. S. Anil Kumar, M. Kareev, L. Gu, D. D. Sarma, P. Shafer, E. Arenholz, J. W. Freeland, L. Li, D. Vanderbilt, and J. Chakhalian, Nano Lett. **21**, 2010 (2021).

[5] X. Liu, S. Singh, B. J. Kirby, Z. Zhong, Y. Cao, B. Pal, M. Kareev, S. Middey, J. W. Freeland, P. Shafer, E. Arenholz, D. Vanderbilt, and J. Chakhalian, Nano Lett. **19**, 8381 (2019).

[6] T. Liang, S. M. Koohpayeh, J. W. Krizan, T. M. McQueen, R. J. Cava, and N. P. Ong, Nat. Commun. **6**, 7611 (2015).

[7] A. W. Kinross, M. Fu, T. J. Munsie, H. A. Dabkowska, G. M. Luke, S. Sachdev, and T. Imai, Phys. Rev. X **4**, 031008 (2014).

[8] Y. Xu, L. S. Wang, Y. Y. Huang, J. M. Ni, C. C. Zhao, Y. F. Dai, B. Y. Pan, X. C. Hong, P. Chauhan, S. M. Koohpayeh, N. P. Armitage, and S. Y. Li, Phys. Rev. X **12**, 021020 (2022).

[9] P. Chauhan, F. Mahmood, H. J. Changlani, S. M. Koohpayeh, and N. P. Armitage, Phys. Rev. Lett. **124**, 037203 (2020).

[10] J. Ye, Z. Zou, and A. Matsushita, Int. J. Hydrog. Energy **28**, 651 (2003).

[11] T. Hanawa, K. Shinkawa, M. Ishikawa, K. Miyatani, K. Saito, and K. Kohn, J. Phys. Soc. Jpn. **63**, 2706 (1994).

[12] P. W. C. Sarvezuk, J. B. M. da Cunha, and O. Isnard, AIP Adv. **10**, 035016 (2020).

[13] D. Prabhakaran, F. R. Wondre, and A. T. Boothroyd, J. Cryst. Growth **250**, 72 (2003).

[14] Maruthi R, S. K. Deshpande, V. Deshmukh, K. Singh, and S. Thota, J. Phys. D: Appl. Phys. **56**, 025501 (2023).

[15] M. E. A. de Dompablo, Y. L. Lee, and D. Morgan, Chem. Mater. **22**, 906 (2010).

[16] T. Wang, T. Ma, T. Ge, S. Shi, H. Ji, W. Li, and G. Yang, J. Alloys Compd. **750**, 428 (2018).

[17] S. Karmakar, A. B. Garg, M. Sahu, A. Tripathi, G. D. Mukherjee, R. Thapa, and D. Behera, J. Appl. Phys. **128**, 215902 (2020).

[18] E. Husson, Y. Repelin, N. Q. Dao, and H. Brusset, J. Chem. Phys. **67**, 1157 (1977).

[19] J. Peña, M. A. Gusmão, and O. Isnard, Phys. Rev. B **103**, 094409 (2021).

[20] C. Heid, H. Weitzel, F. Bourdarot, R. Calemczuk, T. Vogt, and H. Fuess, J. Phys.: Condens. Matter **8**, 10609 (1996).

[21] T. J. S. Munsie, M. N. Wilson, A. Millington, C. M. Thompson, R. Flacau, C. Ding, S. Guo, Z. Gong, A. A. Aczel, H. B. Cao, T. J. Williams, H. A. Dabkowska, F. Ning, J. E. Greedan, and G. M. Luke, Phys. Rev. B **96**, 144417 (2017).

[22] S. Thota, S. Ghosh, R. Maruthi, D. C. Joshi, R. Medwal, R. S. Rawat, and M. S. Seehra, Phys. Rev. B **103**, 064415 (2021).

[23] Maruthi R, S. Ghosh, M. S. Seehra, D. C. Joshi, M. R. Chowdhury, R. Medwal, R. S. Rawat, B. Weise, and S. Thota, J. Phys.: Condens. Matter **33**, 345801 (2021).

[24] I. Yaeger, A. H. Morrish, C. Boumford, C. P. Wong, B. M. Wanklyn, and B. J. Garrard, Solid State Commun. **28**, 651 (1978).

[25] I. Yaeger, A. H. Morrish, and B. M. Wanklyn, Phys. Rev. B **15**, 1465 (1977).

[26] See Supplemental Material at http://link.aps.org/supplemental/10.1103/PhysRevB.108.224430 for analysis of the XPS data, magnetic exchange constants estimated using the Ising model, and data of DFT $+ U$ calculated total energy for different spin configurations in NiNb$_2$O$_6$, which includes Refs. [8,9,53–59].

[27] G. Kresse and J. Furthmüller, Phys. Rev. B **54**, 11169 (1996).

[28] G. Kresse and J. Furthmüller, Comput. Mater. Sci. **6**, 15 (1996).

[29] G. Kresse and D. Joubert, Phys. Rev. B **59**, 1758 (1999).

[30] J. P. Perdew, A. Ruzsinszky, G. I. Csonka, O. A. Vydrov, G. E. Scuseria, L. A. Constantin, X. Zhou, and K. Burke, Phys. Rev. Lett. **100**, 136406 (2008).

[31] H. J. Monkhorst and J. D. Pack, Phys. Rev. B **13**, 5188 (1976).

[32] A. I. Liechtenstein, V. I. Anisimov, and J. Zaanen, Phys. Rev. B **52**, R5467(R) (1995).

[33] T. Hanawa, M. Ishikawa, and K. Miyatani, J. Phys. Soc. Jpn. **61**, 4287 (1992).

[34] C. M. N. Kumar, Y. Xiao, H. S. Nair, J. Voigt, B. Schmitz, T. Chatterji, N. H. Jalarvo, and T. Brückel, J. Phys.: Condens. Matter **28**, 476001 (2016).

[35] L. P. Kadanoff, W. Gotze, D. Hamblen, R. Hecht, E. A. S. Lewis, V. V. P. Ciauskas, M. Rayl, and J. Swift, Rev. Mod. Phys. **39**, 395 (1967).

[36] D. T. Teaney, V. L. Moruzzi, and B. E. Argyle, J. Appl. Phys. **37**, 1122 (1966).

[37] D. T. Teaney, Phys. Rev. Lett. **14**, 898 (1965).

[38] A. R. Miedema, R. F. Wielinga, and W. J. Huiskamp, Phys. Lett. **17**, 87 (1965).

[39] M. E. Fisher, Philos. Mag. **7**, 1731 (1962).

[40] E. E. Bragg and M. S. Seehra, Phys. Rev. B **7**, 4197 (1973).

[41] Maruthi R, M. S. Seehra, S. Ghosh, R. Medwal, R. S. Rawat, B. Weise, E. S. Choi, and S. Thota, J. Phys.: Condens. Matter **34**, 155801 (2022).

[42] S. K. Jena, D. C. Joshi, Z. Yan, Y. Qi, S. Ghosh, and S. Thota, J. Appl. Phys. **128**, 073908 (2020).

[43] V. Narang, D. Korakakis, and M. S. Seehra, J. Magn. Magn. Mater. **368**, 353 (2014).

[44] P. Nordblad, L. Lundgren, E. Figueroa, U. Gafvert, and O. Beckman, Phys. Scr. **20**, 105 (1979).

[45] S. Ghosh, D. C. Joshi, P. Pramanik, S. K. Jena, S. Pittala, T. Sarkar, M. S. Seehra, and S. Thota, J. Phys.: Condens. Matter **32**, 485806 (2020).

[46] P. W. C. Sarvezuk, M. A. Gusmão, J. B. M. da Cunha, and O. Isnard, Phys. Rev. B **86**, 054435 (2012).

[47] J. D. Rall, M. S. Seehra, and E. S. Choi, Phys. Rev. B **82**, 184403 (2010).

[48] S. Kobayashi, S. Mitsuda, M. Ishikawa, K. Miyatani, and K. Kohn, Phys. Rev. B **60**, 3331 (1999).

[49] C. Coulon, H. Miyasaka, and R. Clérac, Struct. Bond **122**, 163 (2006).

[50] P. Pramanik, S. Singh, M. R. Chowdhury, S. Ghosh, V. Sathe, K. M. Rabe, D. Vanderbilt, M. S. Seehra, and S. Thota, Phys. Rev. B **104**, 014433 (2021).

[51] S. Ghosh, S. Singh, D. C. Joshi, P. Pramanik, S. Ghosh, P. K. Mishra, and S. Thota, Phys. Rev. B **98**, 235119 (2018).

[52] S. Ghosh, S. Singh, D. Das, S. Ghosh, P. K. Mishra, and S. Thota, J. Phys.: Condens. Matter **33**, 145504 (2021).

[53] L. Chen, J. Zhang, X. Ren, R. Ge, W. Teng, X. Sun, and X. Li, Nanoscale **9**, 16632 (2017).

[54] M. Yang and R. Rao, J. Mater. Sci. **53**, 15487 (2018).

[55] W. He, X. Li, S. An, T. Li, Y. Zhang, and J. Cui, Sci. Rep. **9**, 10838 (2019).

[56] L. Li, E. Han, L. Zhu, S. Qiao, and C. Du, Ionics **26**, 2655 (2020).

[57] R. Jana, A. Gupta, R. Choudhary, and O. P. Pandey, J. Sol-Gel Sci. Technol. **96**, 405 (2020).

[58] T. E. Jones, T. C. R. Rocha, A. K. Gericke, C. Stampfl, R. Schlogl, and S. Piccinin, Phys. Chem. Chem. Phys. **17**, 9288 (2015).

[59] T. H. Ko, K. Devarayan, M. K. Seo, H. Y. Kim, and B. S. Kim, Sci. Rep. **6**, 20313 (2016).